PROCEEDINGS A

royalsocietypublishing.org/journal/rspa



Research





Cite this article: Kay AF, Durey M, Bush JWM. 2025 Classical pilot-wave dynamics in three dimensions. *Proc. R. Soc. A* **481**: 20240986. https://doi.org/10.1098/rspa.2024.0986

Received: 22 December 2024 Accepted: 30 June 2025

Subject Areas:

applied mathematics

Keywords:

pilot-wave theory, self-propelled particles, chaos and nonlinear dynamics

Author for correspondence:

Matthew Durey
e-mail: matthew.durey@glasgow.ac.uk

Electronic supplementary material is available online at https://doi.org/10.6084/m9.figshare. c.7929110.

THE ROYAL SOCIETY PUBLISHING

Classical pilot-wave dynamics in three dimensions

Adam F. Kay¹, Matthew Durey² and John W. M. Bush¹

¹Department of Mathematics, Massachusetts Institute of Technology, Cambridge, MA 02139, USA ²School of Mathematics and Statistics, University of Glasgow, University Place, Glasgow G12 8QQ, UK

AFK, 0009-0005-0464-940X; MD, 0000-0002-4232-1705; JWMB, 0000-0002-7936-7256

Inspired by the hydrodynamic pilot-wave system and its successes as a basis for hydrodynamic quantum analogues, we present the results of a theoretical investigation of classical pilot-wave dynamics in three dimensions. We consider a particle emitting a spherically symmetric monochromatic wave, then moving in response to the local wave gradient. We demonstrate that, beyond a critical coupling constant, the stationary state destabilizes into a self-propelling state. We compute the quasi-monochromatic form of the accompanying pilot-wave field, and its dependence on the relevant control parameters, specifically the particle inertia and longevity of the pilot-wave field. The similarities between the dynamics arising in the three-dimensional system and its two-dimensional counterpart suggest that many of the quantum features captured in two dimensions will be robust to the transition to three dimensions. We discover a family of dynamical states peculiar to the three-dimensional geometry considered, including helical spin states in which the particle velocity has both angular and rectilinear components. These helical spin states are found to be quantized in both radius of curvature and pitch length and illustrate how classical pilot-wave dynamics may support a feature reminiscent of quantum spin. More exotic dynamical states are also explored and detailed.

1. Introduction

The hydrodynamic pilot-wave system discovered by Yves Couder and Emmanuel Fort in 2005 [1] consists of a millimetric droplet walking along the surface of

© 2025 The Authors. Published by the Royal Society under the terms of the Creative Commons Attribution License http://creativecommons.org/licenses/by/4.0/, which permits unrestricted use, provided the original author and source are credited.

a vibrating bath, self-propelling through a resonant interaction with its accompanying quasimonochromatic 'pilot' wave [1]. The walking-droplet system is of notable interest to the scientific community owing to its ability to capture certain features previously thought to be exclusive to the microscopic quantum realm [2,3]. A key feature of pilot-wave hydrodynamics is that the droplet dynamics are non-Markovian: the bath serves as the memory of the droplet, and the quantum-like features are most pronounced when the pilot wave is most persistent, in the long-memory limit. The ever-growing list of hydrodynamic quantum analogues achieved with the walking-droplet system now includes single-particle diffraction and interference [4–6], quantized orbits [7–10], statistical projection effects [11], Friedel oscillations [12], superradiance [13], Anderson localization [14], surreal trajectories [15] and interaction-free measurement [16]. The pilot-wave hydrodynamic system has thus extended the range of classical systems and prompted a revisitation and redefinition of the boundary between classical and quantum.

The hydrodynamic quantum analogue venture has been bolstered by a number of historical precedents. Specifically, the physical picture engendered in the walking-droplet system, of an oscillating particle interacting with its own wave field, was originally proposed in the 1920s by Louis de Broglie in his double-solution pilot-wave theory of quantum dynamics [17]. The same physical picture also arises in stochastic electrodynamics, according to which quantum particles oscillating at the Compton frequency interact with the electromagnetic quantum vacuum field [18]. Finally, this physical picture has provided the basis for an exploration of hydrodynamically inspired classical field theories of quantum dynamics [19–22].

An often-mentioned shortcoming of the hydrodynamic pilot-wave system is that the droplet motion is effectively confined to a plane, specifically the vibrating bath surface. The droplet motion is discontinuous in the sense that the droplet detaches from the free surface after each bounce. Might this physical picture of classical pilot-wave dynamics be extended to three dimensions, where the particle cannot detach from its pilot wave? We here answer this question in the affirmative through consideration of a theoretical model of an oscillating spherical particle emitting a spherically symmetric wave form.

The walking-droplet system has inspired investigations of other classical pilot-wave systems, some of which are situated in three spatial dimensions. The first consists of a floating object submerged in a stratified fluid [23]. Oscillations in the liquid pressure generate vertical oscillations in the floater that generate internal waves that may propel it forward. It has long been known that acoustic waves can generate oscillations of bubbles submerged in liquids, which may in turn lead to irregular bubble motion [24]. Baudoin and co-authors have recently investigated this acoustic problem theoretically. While they find that spherically symmetric bubble oscillations give rise to a back-reactive force that resists motion [25], self-propulsion of dipolar sources is possible. To date, none of these three-dimensional pilot-wave systems has supported steady rectilinear particle motion, as arises in the walking-droplet system. We here demonstrate that such a state, the existence of which is required for several hydrodynamic quantum analogues, is a robust solution in our model.

In §2, we define the theoretical model of three-dimensional classical pilot-wave dynamics to be considered in our study. We assess the stability of both the stationary state and the steady, self-propelling state, and describe the form of the accompanying pilot-wave field. In §3, we examine a dynamical state particular to three dimensions, a helical spin state, whose robustness is rationalized via stability analysis. In §4, we explore more exotic orbital states revealed through simulation. In §5, we summarize our results by comparing classical pilot-wave dynamics in one, two and three dimensions.

2. Generalized pilot-wave dynamics

A hierarchy of theoretical models have been developed to describe the dynamics of walking droplets [3,26], which necessarily require descriptions of the wave-particle coupling. The bouncing droplet is accelerated by a propulsive force proportional to the local slope of its

guiding wave and decelerated by the drag induced during impact and flight [27,28]. Each impact in turn is marked by the generation of a temporally decaying, circularly symmetric wave form. The global wave form is thus deduced by summing up all such contributions, which requires integration along the particle path. The stroboscopic approximation [29] is based on the assumption of resonance between the droplet and its guiding wave, which enables one to effectively average over the bouncing period and so eliminate the droplet's vertical dynamics from consideration. The resulting horizontal droplet dynamics are those apparent when one strobes the walking-droplet at the Faraday frequency and observes the droplet surfing horizontally on its pilot wave [30].

Bush [2] proposed a parametric generalization of the stroboscopic model, with a view to exploring two-dimensional classical pilot-wave dynamics in parameter regimes inaccessible to experiments, and discovering new quantum features not apparent in the hydrodynamic system. This generalized framework captures the key features of the hydrodynamic system, including a transition from a stationary state to a self-propelling state at a critical memory [31,32]. It also reveals that certain features that are elusive in the hydrodynamic system are robust in different regions of parameter space. For example, in-line speed oscillations with the Faraday wavelength have been observed in certain corners of parameter space [33-35] and are known to provide a robust mechanism for the emergence of quantum-like statistics in several settings [12]. While not the norm in the walking-droplet system, these speed oscillations are a robust feature in the generalized framework [31]. Likewise, irregular jittering motion [31,32] is a rarity in the laboratory but simply found in the generalized framework. The possibility of hydrodynamic spin states, consisting of a droplet executing a circular orbit, its radial motion confined by its wave field, was first noted by Oza et al. [36]. While difficult to capture in the laboratory [37], they too are a robust feature in the generalized framework, arising in the high-memory, lowparticle-inertia limit [38,39]. Finally, the generalized framework has revealed novel dynamics for interacting particle pairs [40,41] and novel statistics for a particle interacting with an oscillatory potential [42]. We here extend this generalized pilot-wave framework to three dimensions with a view to expanding the class of quantum features accessible with classical pilot-wave theory.

(a) Governing equations

The generalized pilot-wave framework in two dimensions describes the evolution of a particle with position $x_p(t)$ at time t that is guided by the slope of its self-generated wave field, h(x, t), and resisted by drag [2,29]. Time-averaging over the particle's vibration period, T (corresponding to the Faraday period in the walking-droplet system), reveals that the particle evolves according to the trajectory equation [29,31]

$$m\ddot{x}_p + D\dot{x}_p = -F\nabla h(x_p, t), \tag{2.1}$$

where m is the particle mass, D is the linear drag coefficient and F is the magnitude of the time-averaged, wave-induced force. The particle generates circularly symmetric Bessel waves along its path, the superposition of which defines the wave field

$$h(x,t) = \frac{A}{T} \int_{-\infty}^{t} J_0(k|x - x_p(s)|) e^{-(t-s)/\tau} ds,$$
 (2.2)

where A is the amplitude of the wave field generated at each moment in time, τ defines the characteristic wave decay time and $k=2\pi/\lambda$ is the wavenumber [29]. In the hydrodynamic experiments, τ is prescribed by the proximity to the Faraday threshold and λ is the Faraday wavelength. For the dynamics of a single particle, the Bessel wave kernel $J_0(k|x-x_p|)$ in (2.2) adequately describes the near-field wave form and so is commonly adopted for its mathematical convenience. While successful in capturing many features of pilot-wave hydrodynamics, the stroboscopic model does have its limitations, including instantaneous wave propagation [26,43–47], which renders it inadequate in modelling droplet–droplet interactions [48,49]. The defining property of the pilot-wave system (2.1) and (2.2) is a feedback mechanism wherein

the past locations of the particle affect its future via the wave field, which acts as a guiding self-potential, the path memory of the system [43].

To extend the generalized pilot-wave framework to three dimensions, we follow its adaptation to one dimension, a theoretical abstraction that necessitated a concomitant change in the wave kernel [32,50]. As $J_0(kr)$ is the bounded circularly symmetric solution of the two-dimensional Helmholtz equation, $(\nabla^2 + k^2)J_0(kr) = 0$, the analogous wave kernel in one dimension was defined as $\cos(k(x-x_p))$ [32,50], with $\cos(kx)$ being the symmetric solution to the Helmholtz equation $(\partial_{xx} + k^2)\cos(kx) = 0$. Similarly, we here define the stroboscopic pilot wave in three dimensions in terms of the spherically symmetric wave kernel $j_0(k|x-x_p|)$, where $j_0(kr)$ is the spherical Bessel function of the first kind with order zero, the bounded axisymmetric solution to the three-dimensional Helmholtz equation, $(\nabla^2 + k^2)j_0(kr) = 0$. The particle position, $x_p(t) = (x_p(t), y_p(t), z_p(t))$, thus evolves according to (2.1) and the wave field is defined as

$$h(x,t) = \frac{A}{T} \int_{-\infty}^{t} j_0(k|x - x_p(s)|) e^{-(t-s)/\tau} ds.$$
 (2.3)

The three-dimensional extension of the stroboscopic model, comprising (2.1) and (2.3), contains the minimal features necessary to produce quantum-like behaviour in a classical pilot-wave system, namely path memory (as prescribed by the time scale τ) and a monochromatic wave field.

(b) Dimensionless trajectory equation

We characterize the dynamics of the free particle in terms of dimensionless variables. Specifically, we scale lengths with the inverse pilot-wavenumber, so $\hat{x} = kx$, time with the memory time at the onset of self-propulsion, $t = \tau_0 \hat{t}$ (where $\tau_0 = \sqrt{3DT/FAk^2}$ [50]), and the pilot wave by its amplitude at the propulsion threshold, $h = \hat{h}A\tau_0/T$. By substituting this rescaling into the pilot-wave system ((2.1) and (2.3)), eliminating the wave field by substituting (2.3) into (2.1) and dropping the overhead carets, we deduce that

$$\kappa_0 \ddot{\mathbf{x}}_p + \dot{\mathbf{x}}_p = 3 \int_{-\infty}^t \frac{\mathbf{j}_1(|\mathbf{x}_p(t) - \mathbf{x}_p(s)|)}{|\mathbf{x}_p(t) - \mathbf{x}_p(s)|} (\mathbf{x}_p(t) - \mathbf{x}_p(s)) e^{-\mu(t-s)} \, \mathrm{d}s, \tag{2.4}$$

which represents the integro-differential trajectory equation governing three-dimensional particle motion. The particle motion is governed by the dimensionless mass $\kappa_0 = m/\tau_0 D$ and the dissipation rate $\mu = \tau_0/\tau$, which is inversely proportional to the time scale over which the particle appreciably interacts with its prior trajectory via the wave field. We define $\Gamma = 1 - \mu$ to capture this notion of path memory, where $\Gamma = 0$ at the onset of particle self-propulsion and $\Gamma = 1$ in the zero-wave-damping, infinite-memory limit. We note that the parameter Γ is analogous to the normalized vibrational forcing in the related hydrodynamic system, with $\Gamma = 1$ corresponding to the Faraday threshold [2,38]. By recasting the pilot-wave system in terms of just two dimensionless parameters, we may characterize all of the various dynamical states arising in the three spatial dimensions through consideration of a two-dimensional parameter space.

(c) Steady propulsion

Beyond the threshold at which the stationary state destabilizes ($\Gamma > 0$), the particle propels in a straight line at a constant speed, guided by the slope of the waves generated along its path. The walking speed, u > 0, depends on the path memory parameter, $\Gamma = 1 - \mu$, as may be established by substituting the ansatz $x_p(t) = ute$ into the trajectory equation (2.4), where e is the unit vector in the direction of particle motion. Specifically, we find that u and μ are related by

$$u = 3 \int_0^\infty j_1(ut)e^{-\mu t} dt,$$
 (2.5)

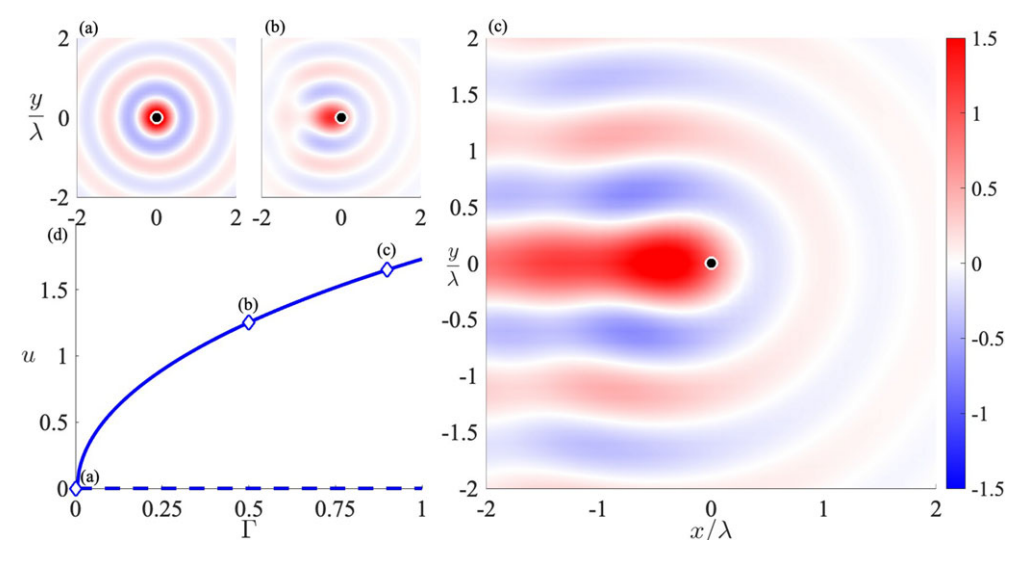


Figure 1. Dependence of the three-dimensional pilot-wave field and particle speed, u, on the dimensionless path memory, Γ . (a) Cross-section of $i_0(r)$, the dimensionless wave field of a stationary bouncer at the walking threshold ($\Gamma=0$). (b) The particle moves at a constant speed for $\Gamma=0.5$. (c) The high-memory regime ($\Gamma=0.9$), where the wave field exhibits an interference pattern downstream of the particle. (d) The dependence of the walking speed (solid curve) on the path memory parameter, Γ (see (2.6)), as initiates from a supercritical pitchfork bifurcation at $\Gamma=0$ [29,50]. Diamonds correspond to the wave fields in (a)–(c). The dashed line at u=0 represents the unstable stationary particle.

whereupon evaluating the integral (the Laplace transform of $j_1(ut)$) determines that u > 0 satisfies

$$u = \frac{u^3}{3} + \mu \arctan \frac{u}{\mu}.$$
 (2.6)

By solving (2.6) numerically, we deduce that the walking speed, u, increases monotonically with $\Gamma = 1 - \mu$, vanishing at the self-propulsion threshold and approaching the upper bounded $u = \sqrt{3}$ in the infinite-memory limit (figure 1). Moreover, the corresponding wave field, h(x,t), exhibits a hemispherical form ahead of the particle with interference in its wake, as is reminiscent of the hydrodynamic system [29,43]. Both of these features are enhanced as the particle speed increases.

Consistent with prior studies of pilot-wave dynamics in two spatial dimensions [29], we find that the particle is neutrally stable to perturbations perpendicular to the line of motion, with the particle returning to steady walking in a new direction after an initial transient (see appendix A for details). It is the perturbations parallel to the direction of motion that yield the richest particle response, with overdamped and underdamped oscillations prevalent as memory increases, analogous to the one- and two-dimensional counterparts of the pilot-wave system [31,32]. At long path memory, the droplet motion destabilizes for $0 < \kappa_0 < \kappa_c$ (where $\kappa_c = \pi/(2\sqrt{3}) \sim 0.907$), corresponding to the upper curve in figure 2a. Beyond this critical threshold, perturbations grow exponentially in time, oscillating over a length scale comparable to the wavelength of the pilot wave [31]. The result is an erratic walking regime (figure 2b), as previously reported in the two-dimensional setting [35,39], with similar features such as in-line speed oscillations over the pilot-wavelength and diffusive behaviour over long times.

Numerical exploration of erratic walking reveals a rich and surprising dynamics beyond the in-line speed oscillations and diffusion seen in two dimensions. For example, the erratic walking can adopt unpredictable, intermittent spiralling motion (figure 3a). The spirals have a diameter close to the pilot-wavelength and persist over a range of times before returning to the less structured erratic state, which can include intervals of rectilinear walking. The coexistence of rectilinear motion and tangled spirals is reminiscent of the 'run and tumble' regime reported for

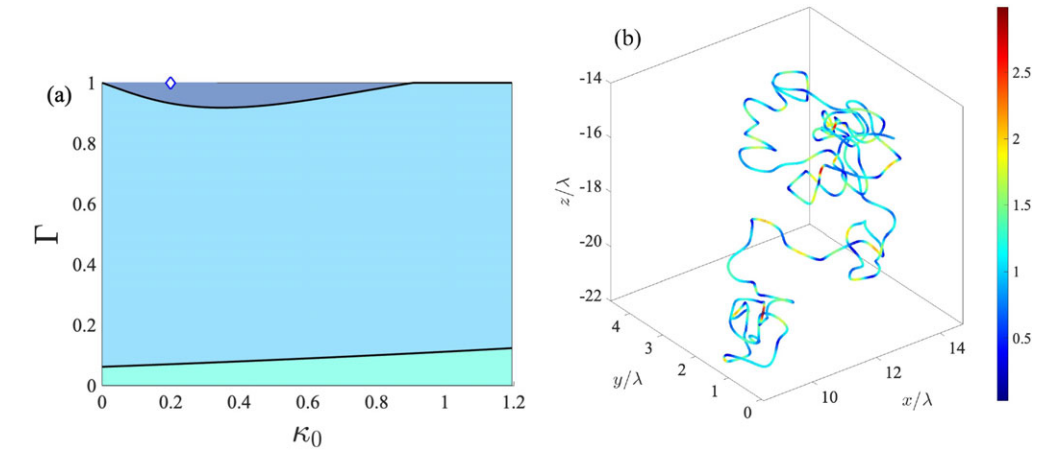


Figure 2. Stability of rectilinear self-propelling states in three-dimensional pilot-wave dynamics. (a) Regime diagram demarcating the stability of the free walker for different values of the dimensionless mass, κ_0 , and memory parameter, Γ . At low memory, the steady walking is stable to overdamped in-line perturbations that decrease monotonically in time (turquoise region). As the memory is increased, the response to in-line perturbations changes from overdamped to underdamped oscillations, leading to damped speed oscillations (light blue region). At high memory and for $0 < \kappa_0 \lesssim 0.907$ (dark blue region), the rectilinear walking state is unstable, leading to an erratic trajectory. (b) Erratic self-propulsion in the high-memory limit ($\Gamma = 1$) for $\kappa_0 = 0.2$. The trajectory is colour-coded according to the dimensionless particle speed. The simulation was performed using a fourth-order Adams—Bashforth time-stepping scheme [9].

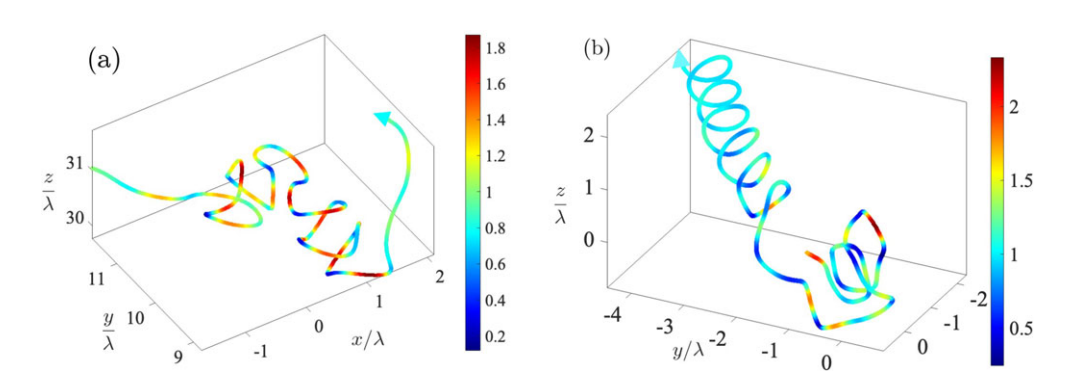


Figure 3. Emergence of helical spin states in three-dimensional pilot-wave dynamics. (a) Transient coiling trajectory in the erratic regime for $\kappa_0=0.45$ and $\Gamma=0.97588$. (b) Spontaneous formation of a stable helical spin state for $\Gamma=1$ and $\kappa_0=0.2$. The simulations were performed using a fourth-order Adams–Bashforth time-stepping scheme [9].

two-dimensional pilot-wave systems [35,39]. These spirals mark a transition between an unstable, erratic self-propelling state and a stable helical spin state. As shown in figure 3*b*, the erratic state can spontaneously transition to a helical state, particular to three dimensions.

3. Helical spin states

Our analysis in §2 demonstrates that the dynamics of a stationary or steadily propelling particle is in many respects analogous to that in the hydrodynamic system [29,31], in which a particle navigates its two-dimensional pilot-wave field in a plane. Peculiar to three dimensions is the steady helical motion (§3(a)), which may be thought of as a three-dimensional extension of planar

spin states [38]. We proceed by presenting a systematic study of the existence and stability of these steady helical states, as illustrated by numerical simulations in §4.

(a) Steady helical motion

We consider the steady helical motion of a particle executing circular loops at radius r_0 and angular frequency ω , while simultaneously translating along an axis parallel to the unit vector e_z at speed v. The particle motion may be expressed $x_p(t) = r_0e_r(t) + vte_z$, where $e_r(t) = \cos(\omega t)e_x + \sin(\omega t)e_y$ is the radial unit vector and $e_\theta(t) = -\sin(\omega t)e_x + \cos(\omega t)e_y$ is its angular counterpart, with $\{e_x, e_y, e_z\}$ forming a fixed orthonormal basis. By substituting this ansatz into the trajectory equation (2.4) and considering the force balance in the radial, tangential and vertical directions, respectively, we deduce that

$$-\kappa_0 r_0 \omega^2 = 3r_0 \int_0^\infty \frac{\mathbf{j}_1(\mathcal{D}(t))}{\mathcal{D}(t)} (1 - \cos(\omega t)) e^{-\mu t} dt, \tag{3.1a}$$

$$r_0 \omega = 3r_0 \int_0^\infty \frac{\mathbf{j}_1(\mathcal{D}(t))}{\mathcal{D}(t)} \sin(\omega t) e^{-\mu t} dt$$
(3.1b)

and

$$v = 3v \int_0^\infty \frac{\mathbf{j}_1(\mathcal{D}(t))}{\mathcal{D}(t)} t e^{-\mu t} dt, \tag{3.1c}$$

where

$$\mathcal{D}(t) = \sqrt{2r_0^2(1 - \cos(\omega t)) + v^2 t^2}$$
(3.2)

denotes the distance between the particle's current position and that at a time t in the past. We solve (3.1) numerically to determine r_0 , ω and v (the orbital radius, angular frequency and translation speed, respectively), for given κ_0 and μ . Notably, (3.1a) and (3.1b) are satisfied by $r_0=0$, with (3.1c) then supplying the force balance for a particle moving in a straight line at a constant speed, as detailed in §2(c). Furthermore, (3.1c) is satisfied by v=0, corresponding to a planar spin state, the existence and stability of which have been rationalized for the two-dimensional pilot-wave system [38] and will be briefly characterized in §3(d) for the spherical wave kernel considered in our investigation.

As is the case for circular orbits in two spatial dimensions [7], the monochromatic nature of the guiding wave field is likely to impose geometric constraints on the permissible solutions to the steady helical equations (3.1), particularly at high memory ($\mu \ll 1$). To gain insight into the form of the pilot wave accompanying steady helical motion (as computed by substituting $x_p(t)$ into the dimensionless counterpart of equation (2.3)), we present cross-sectional slices of h(x,t) in figure 4. In figure 4a, we see in the xz-plane the wave field accompanying the particle, whose form and amplitude are prescribed by the path memory. The oscillations in the pilot wave in the direction of propagation are thus likely to restrict the permissible values of the helical pitch length, Λ . In figure 4b, we see the wave field in the xy-plane perpendicular to the direction of propagation, in which the wave field is similar to that emerging for orbital dynamics in two spatial dimensions [7,36]. We thus anticipate that, as in their two-dimensional orbital counterpart, helical states will be quantized in their radial extent.

(b) Emergence of double quantization

For different values of κ_0 and μ , a large number of helical states may be found by solving the force balance equations (3.1). At low memory (Γ < 0.7), the wave field decays too quickly to be able to support steady helical states. However, as the memory is increased, a series of helical states emerge, at the helical existence boundaries detailed in figure 5, in a manner similar to spin states in two dimensions [38]. Each helical state is associated with exactly one existence boundary, and we distinguish these boundaries in terms of the helix's radius, r_0 , and pitch length, Λ (as indicated in figure 4). Notably, the critical memory of each existence boundary increases with the dimensionless mass, κ_0 , in a manner similar to two-dimensional spin states, with helical states

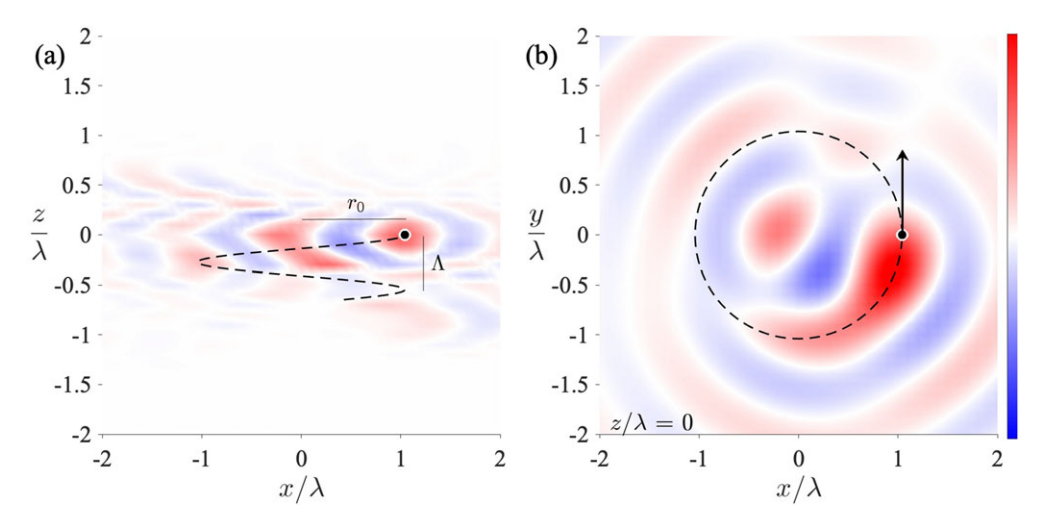


Figure 4. The pilot-wave field and particle trajectory (dashed curves) for a stable helical state arising when $\Gamma=0.865$ and $\kappa_0=0.01$. The radius, angular frequency and translation speed are $r_0=1.04\lambda$, $\omega=0.2$ and v=0.14, respectively, and satisfy the steady helical equations (3.1). (a) Cross-section of the wave field through the *x-z* (y=0) plane. The particle moves counter-clockwise and the pitch length is denoted by Λ . (b) Cross-section of the wave field in the *x-y* (z=0) plane. Positive and negative values of h(x,t) are denoted in red and blue, respectively.

being most prevalent in the overdamped ($\kappa_0 = 0$) limit. We rationalize the shape of the existence boundaries in terms of the particle's tendency to be propelled outwards when inertial effects are more pronounced, and so the pilot wave needs to be of larger amplitude to confine the particle, as is achieved at higher memory.

The structure of the helical solutions in figure 5 and the influence of the monochromatic pilot wave on both the helix's radius and pitch (figure 4) hint at the possibility of a double quantization emerging for these states. To test this hypothesis, we characterize the helical states in terms of their pitch length, Λ , and radius of curvature, R. The pitch length for a steady helical state is defined as the change in particle position over one loop, namely $\Lambda = \mathcal{D}(2\pi/\omega) = 2\pi v/\omega$ (see (3.2)). In terms of the wavelength of the pilot wave, which is $\lambda = 2\pi$ in dimensionless variables, the pitch length satisfies $\Lambda/\lambda = v/\omega$. The pitch length vanishes for planar spin states, v = 0, but increases with axial speed, v. We anticipate that the monochromatic form of the pilot wave will restrict the accessible values of the pitch length for steady helical motion (figure 4a).

The radius of curvature of a three-dimensional trajectory is defined as

$$R = \frac{|\dot{x}_p|^3}{\sqrt{|\dot{x}_p|^2 |\ddot{x}_p|^2 - (\dot{x}_p \cdot \ddot{x}_p)^2}},$$

where we note that the velocity and acceleration are orthogonal for steady helical motion, and so $\dot{x}_p \cdot \ddot{x}_p = 0$. The radius of curvature thus simplifies in this case to $R = |\dot{x}_p|^2 / |\ddot{x}_p|$, or

$$R = r_0 \left(1 + \frac{v^2}{r_0^2 \omega^2} \right). \tag{3.3}$$

When v = 0, the radius of curvature is simply the radius of the planar spin state. For $v \neq 0$, the translational velocity along the axis of the helix induces a decrease in curvature; consequently, $R > r_0$.

We present in figure 6 the solutions to the helical equations (3.1), characterized in terms of radius of curvature, R, and pitch length, Λ . In accordance with the existence curves in figure 5, each helical solution curve forms from a saddle-node bifurcation (at the left-most tip of each solution curve), giving rise to a pair of helical spin states. The radius of curvature tends to

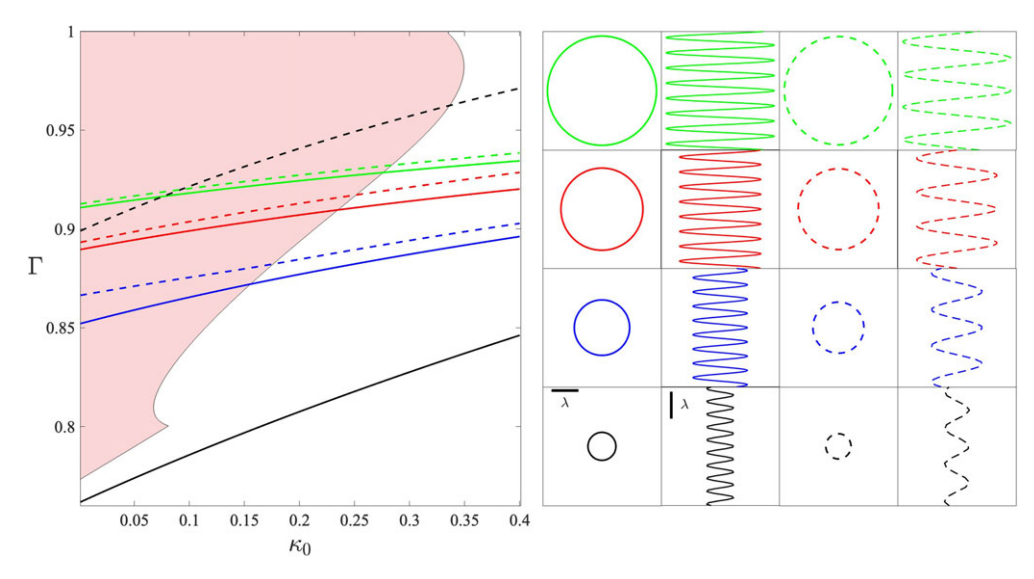


Figure 5. Double quantization in radius of curvature, R, and pitch length, Λ , for the first four helical spin states. We characterize the various helical states by the nomenclature (n, ℓ) , with n and ℓ denoting the radial and pitch quantization numbers, respectively. The solid and dashed curves in the (κ_0, Γ) -plane (left) correspond to the existence thresholds for pitch levels $\ell=1$ and $\ell=2$, respectively, and are overlaid on the stability region for the (1,1) helical state (light red, see figure 7). The radial quantization level is denoted by the curve colour, with n=1 in black, n=2 in blue, n=3 in red, and n=4 in green. Each helical state exists above the corresponding curve in the (κ_0, Γ) -plane. The various helical states are visualized in the legend (right), with each trajectory corresponding to that on the existence line at $\kappa_0 = 0$. The radial quantization number, n, increases from bottom to top, and the pitch length number, ℓ , increases from left to right. The first and third columns are the axial view of the helix, and the second and fourth columns present the corresponding side view. All panels are in proportion, with the pilot-wavelength denoted by the scale bar.

increases with memory for one solution, and decreases for the other (figure 6a), giving rise to the characteristic 'tongue' shape. However, there are also helical states for which the solution curve is more pin-shaped, with very little variation in the radius of curvature with increasing memory. The corresponding pitch length follows a similar progression, with both pin- and tongue-shaped stability curves (figure 6b). At high memory, a wealth of different helical states exist; we present in figure 6 only those with $R/\lambda < 2.5$ and $\Lambda/\lambda < 5.5$.

To untangle this plethora of solution curves, we present in figure 6c the values of the radius of curvature and pitch length on the existence boundary, corresponding to the smallest memory along each solution curve. Despite the complexity apparent in figures 6a,b, we see that a remarkably simple structure emerges. Specifically, the radius of curvature on the existence boundary is very close to a half-integer multiple of the pilot-wavelength ($R \approx n\lambda/2$ with n > 1an integer), similar in form to the emergence of quantized spin states in two dimensions [38]. A quantization in pitch length also emerges, with the solution along the existence boundary lying close to the lines $\Lambda = (\ell - \frac{1}{2})\lambda$ for integers $\ell \ge 1$. We may thus characterize the onset of helical states in terms of a double quantization in radius of curvature and pitch length, which we enumerate in terms of the lattice of 'quantum numbers' n and ℓ , respectively.

Notably, the lattice of quantum numbers is not fully populated. For a fixed value of the radial number, n, only the smallest pitch numbers, ℓ , are accessible, with the range of ℓ increasing with n(see the grey dashed line in figure 6c). We conclude that helical states cannot be highly 'stretched' in the direction of propagation. However, the pitch length can be small relative to the radius of curvature, corresponding to wide, slowly propagating helical states. The most extreme example is the planar spin state with v = 0, for which the pitch length is zero and yet the radius may be arbitrarily large [38].

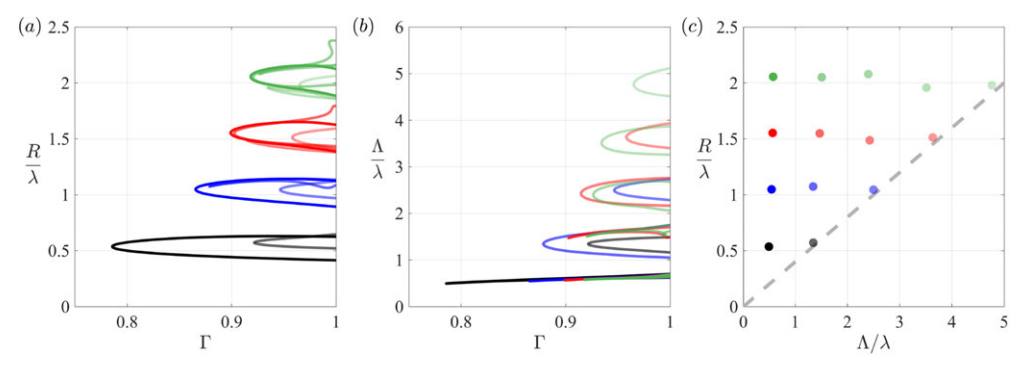


Figure 6. Bifurcation curves for the double quantization of the first four helical states with $\kappa_0=0.1$, as shown in figure 5. The radial quantization number is denoted by the colour of the curve, with n=1 in black, n=2 in blue, n=3 in red and n=4 in green. The pitch quantization number is denoted by the shade of the curve, with $\ell=1$ corresponding to the darkest curves and $\ell=5$ to the lightest. (a) Dependence of the radius of curvature, R, on the memory parameter, Γ . (b) Dependence of the pitch length, Λ , on Γ for the same helical states as in panel (a). (c) The double quantization between radius of curvature and pitch length at the minimum value of the memory parameter, Γ , along each bifurcation curve in panels (a,b), corresponding to the existence curves in figure 5. The points lie roughly on a grid with helical solutions confined to the region above the dashed grey line, indicating that larger pitch lengths are possible only if the radius of curvature is sufficiently large.

Linear stability analysis

Having established the existence of helical states and their corresponding double quantization in radius of curvature and pitch length, we now investigate their robustness to small perturbations, from which we can assess the relative likelihood of various helical states emerging in the evolution of the free particle. To do so, we employ linear stability analysis, extending the framework developed by Oza et al. [36,38] to three spatial dimensions. Using Laplace transforms, we reduce the stability problem to that of finding complex roots of the system's transfer function, from which we may determine the long-time perturbation growth or decay rates, analogous to eigenvalues for non-hereditary systems.

To assess the linear stability of helical states, we first recast the particle trajectory equation (2.4) in cylindrical polar coordinates, namely $x_p(t) = r_p(t)e_r(t) + z_p(t)e_z$, with radial and tangential unit vectors $e_r(t) = \cos \theta_p(t)e_x + \sin \theta_p(t)e_y$ and $e_\theta(t) = -\sin \theta_p(t)e_x + \cos \theta_p(t)e_y$, respectively. By projecting onto the basis $\{e_r, e_\theta, e_z\}$, we derive the system of equations

$$\kappa_0(\ddot{r}_p - r_p\dot{\theta}_p^2) + \dot{r}_p = 3\int_{-\infty}^t \frac{\mathbf{j}_1(\mathcal{D}(t,s))}{\mathcal{D}(t,s)} [r_p(t) - r_p(s)\cos(\theta_p(t) - \theta_p(s))] e^{-\mu(t-s)} \,\mathrm{d}s + \epsilon c_r\delta(t), \tag{3.4a}$$

$$\kappa_0(r_p\ddot{\theta}_p + 2\dot{r}_p\dot{\theta}_p) + r_p\dot{\theta}_p = 3\int_{-\infty}^t \frac{\mathbf{j}_1(\mathcal{D}(t,s))}{\mathcal{D}(t,s)} [r_p(s)\sin(\theta_p(t) - \theta_p(s))] e^{-\mu(t-s)} ds + \epsilon r_0c_\theta\delta(t)$$
(3.4b)

and
$$\kappa_0 \ddot{z}_p + \dot{z}_p = 3 \int_{-\infty}^t \frac{\mathbf{j}_1(\mathcal{D}(t,s))}{\mathcal{D}(t,s)} [z_p(t) - z_p(s)] e^{-\mu(t-s)} \, \mathrm{d}s + \epsilon c_z \delta(t), \tag{3.4c}$$

where $\mathcal{D}(t,s) = |x_p(t) - x_p(s)|$ denotes the distance between the particle's position at times t and s, where s < t. In terms of cylindrical polar coordinates,

$$\mathscr{D}(t,s) = \sqrt{r_p^2(t) + r_p^2(s) - 2r_p(t)r_p(s)\cos(\theta_p(t) - \theta_p(s)) + (z_p(t) - z_p(s))^2}.$$

Finally, we have introduced in (3.4) a perturbation to the trajectory at time t = 0 in terms of a Dirac delta function, $\delta(t)$, where c_r , c_θ and c_z are O(1) constants and $0 < \epsilon \ll 1$ controls the magnitude of the perturbation.

We linearize (3.4) about a helical solution of radius r_0 , angular frequency ω and translation velocity v, where r_0 , ω and v solve the helical force balance equations (3.1). We thus express the particle's trajectory as

$$r_p(t) = r_0 + \epsilon r_1(t)H(t), \quad \theta_p(t) = \omega t + \epsilon \theta_1(t)H(t), \quad \text{and} \quad z_p(t) = vt + \epsilon z_1(t)H(t), \quad (3.5)$$

where $r_1(t)$, $\theta_1(t)$ and $z_1(t)$ are the perturbed radial, angular and vertical components, and H(t)is the Heaviside step function. We impose that the particle's position is continuous across the perturbation at t = 0, corresponding to $r_1(0) = \theta_1(0) = z_1(0) = 0$. However, the delta forcing in (3.4) gives rise to a velocity jump across the perturbation, resulting in the initial conditions $\dot{r}_1(0) = c_r/\kappa_0$, $\dot{\theta}_1(0) = c_\theta/\kappa_0$ and $\dot{z}_1(0) = c_z/\kappa_0$. We substitute (3.5) into (3.4) and retain terms only of size $O(\epsilon)$, from which we deduce that (for t > 0) $r_1(t)$, $\theta_1(t)$ and $z_1(t)$ evolve according to

$$\kappa_0(\ddot{r}_1 - r_1\omega^2 - 2r_0\omega\dot{\theta}_1) + \dot{r}_1 = 3[a_{11}r_1 + (b_{11}*r_1) + a_{12}r_0\theta_1
+ (b_{12}*r_0\theta_1) + a_{13}z_1 + (b_{13}*z_1)],$$

$$\kappa_0(r_0\ddot{\theta}_1 + 2\dot{r}_1\omega) + r_1\omega + r_0\dot{\theta}_1 = 3[a_{21}r_1 + (b_{21}*r_1) + a_{22}r_0\theta_1 + (b_{22}*r_0\theta_1)$$
(3.6a)

$$+ a_{23}z_1 + (b_{23} * z_1)]$$
(3.6b)

and

$$\kappa_0 \ddot{z}_1 + \dot{z}_1 = 3[a_{31}r_1 + (b_{31} * r_1) + a_{32}r_0\theta_1
+ (b_{32} * r_0\theta_1) + a_{33}z_1 + (b_{33} * z_1)],$$
(3.6c)

where the constants a_{ij} and functions $b_{ij}(t)$ are defined in appendix B. Notably, equation (3.6) forms a linear system of integro-differential equations, where the influence of path memory on the evolution of the perturbed particle trajectory is characterized by the convolution terms, specifically those of the form $(f * g)(t) = \int_0^t f(s)g(t-s) ds$ for given functions f(t) and g(t).

To reduce the linearized equations (3.6) to a more amenable form, we take their Laplace transforms and deduce algebraic equations for $\widehat{R}(s) = \mathcal{L}[r_1](s)$, $\widehat{\Theta}(s) = \mathcal{L}[\theta_1](s)$ and $\widehat{Z}(s) = \mathcal{L}[\theta_1](s)$ $\mathcal{L}[z_1](s)$, where $\mathcal{L}[f](s) = \int_0^\infty f(t) e^{-st} dt$ denotes the Laplace transform. By accounting for the initial conditions when applying the Laplace transforms to derivatives, we obtain the system of algebraic equations

$$\begin{pmatrix} A_{11}(s) & A_{12}(s) & A_{13}(s) \\ A_{21}(s) & A_{22}(s) & A_{23}(s) \\ A_{31}(s) & A_{32}(s) & A_{33}(s) \end{pmatrix} \begin{pmatrix} \widehat{R}(s) \\ r_0 \widehat{\Theta}(s) \\ \widehat{Z}(s) \end{pmatrix} = \begin{pmatrix} c_r \\ r_0 c_\theta \\ c_z \end{pmatrix}, \tag{3.7}$$

where we define the functions $A_{ij}(s) = C_{ij}(s) - 3a_{ij} - 3B_{ij}(s)$ in terms of the constants a_{ij} and Laplace transforms $B_{ij}(s) = \mathcal{L}[b_{ij}](s)$, with

$$C_{11}(s) = \kappa_0(s^2 - \omega^2) + s$$
, $C_{12}(s) = -2\kappa_0 \omega s$, $C_{21}(s) = 2\kappa_0 \omega s + \omega$, $C_{22}(s) = \kappa_0 s^2 + s$ and $C_{33}(s) = \kappa_0 s^2 + s$,

and all other C_{ij} terms being equal to zero.

The long-time exponential growth or decay of a perturbed trajectory is governed by the poles of $\widehat{R}(s)$, $r_0\widehat{\Theta}(s)$ and $\widehat{Z}(s)$, which correspond to the roots of det A(s), where A(s) is the 3×3 matrix in (3.7) with elements $A_{ii}(s)$. Notably, there are trivial eigenvalues associated with the various invariant properties of helical trajectories: specifically, s = 0 is a double root of det A(s), with one root reflecting temporal invariance and the other corresponding to the translation of the helix in the propagation direction, denoted by the unit vector e_z . Furthermore, $\det A(s)$ has a pair of double roots at $s = \pm i\omega$, with one complex conjugate pair corresponding to translational invariance in the plane perpendicular to e_z and the other complex conjugate pair corresponding to invariance

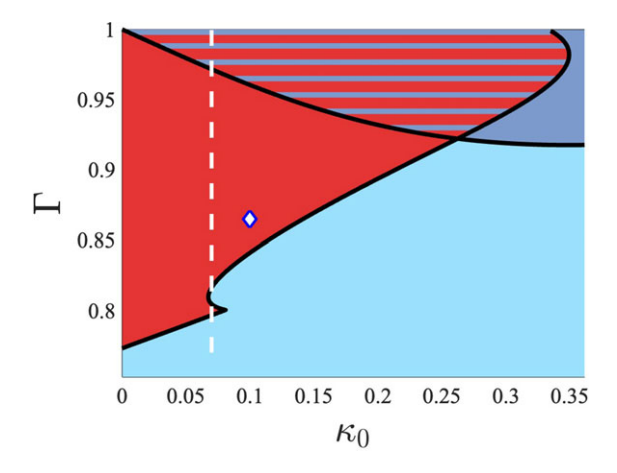


Figure 7. Regime diagram illustrating how the dynamics of a free particle depends on the dimensionless mass, κ_0 , and memory parameter, Γ , in the high- Γ , low- κ_0 corner of figure 2. The red region specifies all values of κ_0 and Γ for which the helical spin state of smallest radius and pitch is stable. The horizontal red and lavender lines represent co-existence of helical spin and erratic walking. The diamond gives the location of the spin state depicted in figure 4, while the white dashed line corresponds to the Γ values for the bifurcation curves given in figure 8.

under rotations of e_z . As the stability of the helical state depends on the non-trivial roots of $\det A(s)$, we define the stability function

$$F_{\text{helix}}(s) = \frac{\det A(s)}{s^2(s^2 + \omega^2)^2},$$

which is analytic for $Re(s + \mu) > 0$. The helical state is stable if all the roots of $F_{helix}(s)$ have a negative real part, and unstable otherwise.

Of the numerous helical states identified in §3(b), only the helix with smallest radius (n = 1) and smallest pitch length ($\ell = 1$) is found to be stable in the absence of external forces. Akin to spin states in two dimensions, the helical state is stable only for small dimensionless mass and relatively high memory, with the stability region in the (κ_0, Γ) -plane detailed in figure 7 (see also the shaded region in figure 5, which lies above the corresponding existence curve). Remarkably, stable helical states may be found even for arbitrarily high memory, including for the limiting case of $\Gamma = 1$, for which the spatial decay of the wave kernel ensures that all integrals in the stability problem converge even in the absence of wave damping (see appendix B). This behaviour differs from two-dimensional spin states, for which the repeated looping of the particle along the same circular path prompts instability at high memory [38]. We note also that the helical stability region extends over the interval $\kappa_0 < 0.347$, and so exceeds that of two-dimensional spin states [38]. The extent of this stability region highlights the robustness of helical spin states, and rationalizes their spontaneous formation in figure 3b.

We note that the helical stability boundary has a sharp kink near $(\kappa_0, \Gamma) = (0.08, 0.8)$, which is associated with a change of instability frequency. This transition gives rise to a particularly complex series of instabilities along the solution curve near this point, which we visualize in figure 8 for $\kappa_0 = 0.07$. When the memory slightly exceeds the existence boundary, the helical state with larger radius is unstable with a monotonically growing perturbation (as is typical of a saddle-node bifurcation) and the helical state with smaller radius is unstable to wobbling perturbations. As memory is increased (tracing along the white dashed line in figure 7), the spin state with smaller radius is stabilized close to $\Gamma = 0.8$. However, increasing memory further leads to a second wobbling instability, corresponding to the interval in which the white line lies above the kink (over the light blue region) in figure 7. This instability is eventually suppressed at high memory, and the helical state is stable up to and including $\Gamma = 1$. These transitions in stability

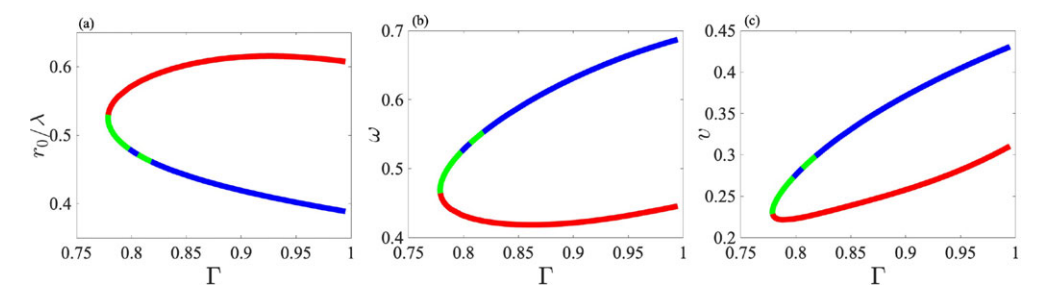


Figure 8. The dependence of the helical state $(n, \ell) = (1, 1)$ on the dimensionless memory parameter, Γ . Bifurcation curves for $\kappa_0 = 0.07$, tracing the white dashed line in figure 7. The bifurcation curves parametrize the helical states by their (a) radius, r_0 , (b) angular frequency, ω , and (c) helical translation speed, υ . The curves are colour-coded according to the linear stability of the helical state. Stable orbits arise on the blue portions of the curve (which overlie the red region in figure 7), and monotonic and oscillatory instabilities on the red and green portions, respectively. There exists a pair of helical states at high memory: the helix with smaller radius and faster translation speed is stable, while the helix with larger radius and smaller translation speed is monotonically unstable. The vertex of the 'tongue' in each panel lies on the existence line for the helical spin state (figure 5), corresponding to $\Gamma_c = 0.7841$ for $\kappa_0 = 0.07$.

are also apparent in the bifurcation curves for the orbital frequency, ω , and translation speed, v, where we note that the solution with smaller radius corresponds to the branch for which ω and vare larger.

Planar spin states

As noted in §3(a), the solution v = 0 to the force balance equations (3.1) gives rise to orbital particle motion confined to a plane and so may be regarded as the pitch number $\ell=0$ for quantized helical states. The radius, r_0 , and angular frequency, ω , of the circular orbits may then be deduced from equations (3.1a)–(3.1b) by setting v = 0, with the stability of the planar spin state likewise being inferred from its helical counterpart. Specifically, the functions A_{13} , A_{23} , A_{31} and A_{32} all vanish when v = 0, with the Laplace transforms of radial and angular perturbations satisfying

$$\begin{pmatrix} A_{11}(s) & A_{12}(s) \\ A_{21}(s) & A_{22}(s) \end{pmatrix} \begin{pmatrix} \widehat{R}(s) \\ r_0 \widehat{\Theta}(s) \end{pmatrix} = \begin{pmatrix} c_r \\ r_0 c_\theta \end{pmatrix}$$

and perturbations perpendicular to the plane being governed by the roots of the transfer function $A_{33}(s)$. In contrast to the two-dimensional system [38], we find that all planar spin states are unstable in their plane of motion. The absence of stable planar spin states might be attributed to the increased spatial decay of the wave kernel in three dimensions, which cannot provide a sufficient inward radial force to stabilize small perturbations. Nevertheless, one expects that in three dimensions as in two, planar spin states may be stabilized by the application of an external confining force [51].

4. Exotic states

The two-dimensional generalized pilot-wave framework is known to exhibit a number of exotic dynamics in different corners of the (κ_0, Γ) parameter space. For example, stable wobbling and precessing spin states emerge just outside the spin state stability region, even in the absence of a confining force [39]. Motivated by this richness, we hunt for similar wobbling dynamics in three dimensions by simulating the stroboscopic trajectory equation (2.4) using a fourth-order Adams-Bashforth time-stepping scheme similar to that developed by Oza et al. [9]. Upon perturbing a weakly unstable helical state at time t = 0, we identify the emergence of stable wobbling helical motion as time increases (figure 9), in which the radius of curvature and speed both oscillate

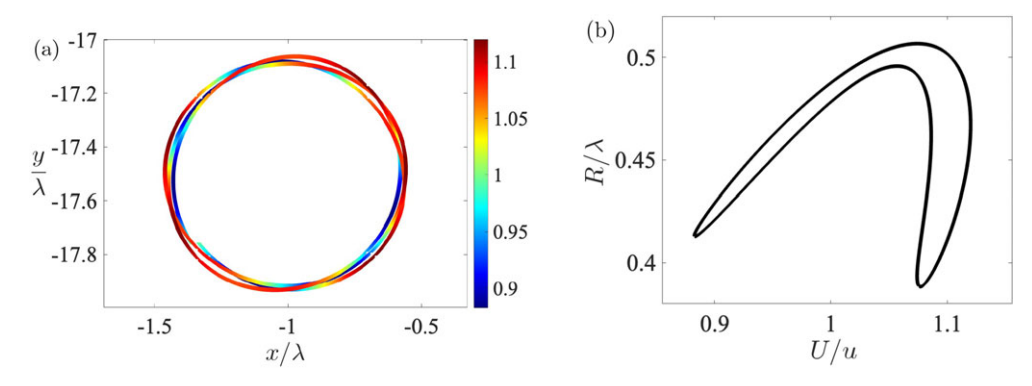


Figure 9. Wobbling helical state for $\kappa_0 = 0.25$ and $\Gamma = 0.90787$. (a) The helical state wobbles about its symmetry axis, with periodic velocity variations. The trajectory is colour-coded by its speed relative to the steady propulsion speed for the given parameters. (b) The limit cycle for the wobbling helical state characterized in terms of its speed, $U = |\dot{x}_p|$, and radius of curvature, R. Here U = 1.6575 is the steady propulsion speed.

periodically in time, with variations on the order of 10%. The existence of these stable helical wobbling states hints at the possibility of numerous wobbling helical states emerging when the particle moves in response to a confining force, as is known to be the case in two dimensions [9,10,52].

As indicated by the regime diagram in figure 7, rectilinear motion is the dominant state of the free particle, as is also the case for the two-dimensional generalized pilot-wave system [39]. Also similar to the two-dimensional system, exotic states are observed in the low-particle inertia, high-memory regime. Here, erratic walking co-exists with stable helical spin states, giving rise to various forms of complex dynamics. These include random walks, either confined to the plane or exploring three-dimensional space (figure 2b), intermittent coiling trajectories (figure 3a), the spontaneous formation of helical states from a random walk (figure 3b) and exotic trajectories arising due to the imposition of relic wave fields. The latter case is implemented by specifying an initial trajectory of the particle, which effectively preconditions the wave field, creating a space-filling potential that the particle then explores.

Presented in figure 10 are three separate systems in which the particle interacts with a wave field generated by imposing the initial particle path. Specifically, we initialize with a helical trajectory in figure 10a and rectilinear motion in figures 10b,c. These imposed trajectories generate the associated wave potential, and the subsequent particle dynamics. The initial helical wave field in figure 10a prompts a spontaneous reversal of the particle, which coils backwards along the imposed helix before then spiralling towards a stable helical state. Initializing with an anomalously low-speed walking speed at $\Gamma=1$ generates a highly structured potential that the particle explores. If the initial propulsion speed is sufficiently small, the self-potential is nearly spherically symmetric, and the particle is largely confined to a spherical shell (figure 10b). If the initial speed is larger, the self-potential is circularly symmetric, and the particle is confined to a cylindrical shell (figure 10c). In both instances, the diameter of the confining shells is prescribed by the pilot-wavelength. As the simulations are done in the infinite-memory limit ($\Gamma=1$), the particle appears to be restricted to these shells indefinitely. The richness of these memory-induced, hereditary dynamics suggests the likelihood of a variety of exotic states in three-dimensional pilot-wave systems.

5. Discussion

Pilot-wave hydrodynamics has provided a platform for realizing quantum behaviour on the macroscopic scale, and so for redefining the boundaries between classical and quantum systems

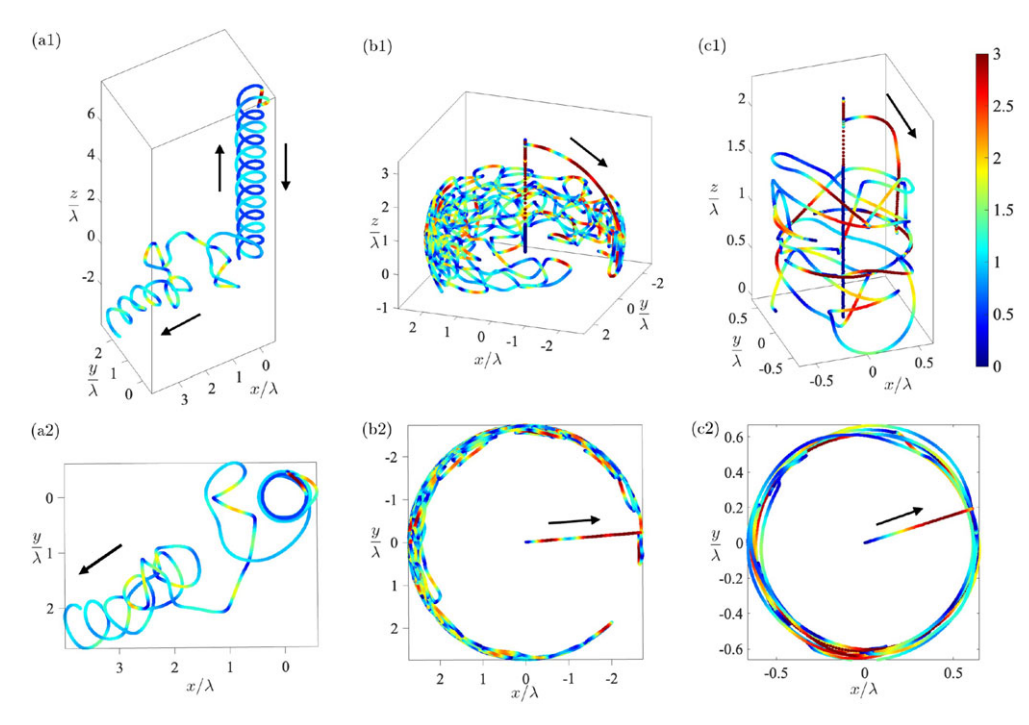


Figure 10. Exotic trajectories with an imposed initial path. (a1) A particle initialized in an imposed helical trajectory at $\Gamma=1$ and $\kappa_0=0.27$ with parameters $r_0=0.43\lambda$, $\omega=0.306$, and $\upsilon=0.352$. Upon release, the particle reverses its path, forming a double helix and eventually stabilizing into a new helical spin state. (a2) The same plot projected onto the x-y axis. (b1) A rectilinear walker initialized in the +z direction with an anomalously low walking speed of 0.0071u, where u=1.732 is the free walking speed and $\kappa_0=0.32$. After release, the particle reaches a maximum speed of 38.627 before being confined to a spherical shell with radius $\approx 2.7\lambda$. The corresponding x-y projection is shown in (b2). (c1) A similar rectilinear walker is initialized with speed 0.0705u and $\kappa_0=0.32$. The particle reaches a maximum speed of 9.63 before being confined to a cylindrical shell, with the x-y projection depicted in (c2). The time step is set to be 2^{-6} or smaller for all simulations, with robustness verified by benchmarking against steady and perturbed rectilinear and helical states.

[2]. The generalized pilot-wave framework has provided a vehicle for exploring two-dimensional pilot-wave dynamics in parameter regimes inaccessible to the walking-droplet system [31]. We have here extended this framework to consider three-dimensional pilot-wave dynamics, in which a vibrating particle generates a wave with a spherical Bessel function form, then moves in response to wave gradients. A comparison of the salient features of theoretical models of pilotwave dynamics in one through three dimensions is provided in table 1. The dependence of the dynamics of the free particle motion in three dimensions on the dimensionless mass, κ_0 , and memory, Γ , is summarized in figure 11. Pilot-wave dynamics in three dimensions has both similarities and differences with its two-dimensional counterpart.

As in the two-dimensional case, the behaviour of the free particle is characterized in terms of two dimensionless parameters that prescribe the dimensionless particle inertia, κ_0 , and the system memory, Γ . The trajectory equation supports a stationary solution that becomes unstable to perturbations and transitions to a self-propelling state, marked by rectilinear motion at constant speed, at the walking threshold $\Gamma = 0$. The resulting self-propelling state is stable for a wide range of κ_0 and Γ and exhibits neutrally stable responses to perturbations orthogonal to the direction of motion. The response to parallel perturbations can be either overdamped or underdamped. For high memory and low particle inertia (below approximately $\kappa_0 = 0.9$), the walking state destabilizes and the particle trajectory becomes erratic. As in the two-dimensional case, intriguing periodic and quasi-periodic states arise in the low inertia, high memory corner of parameter space.

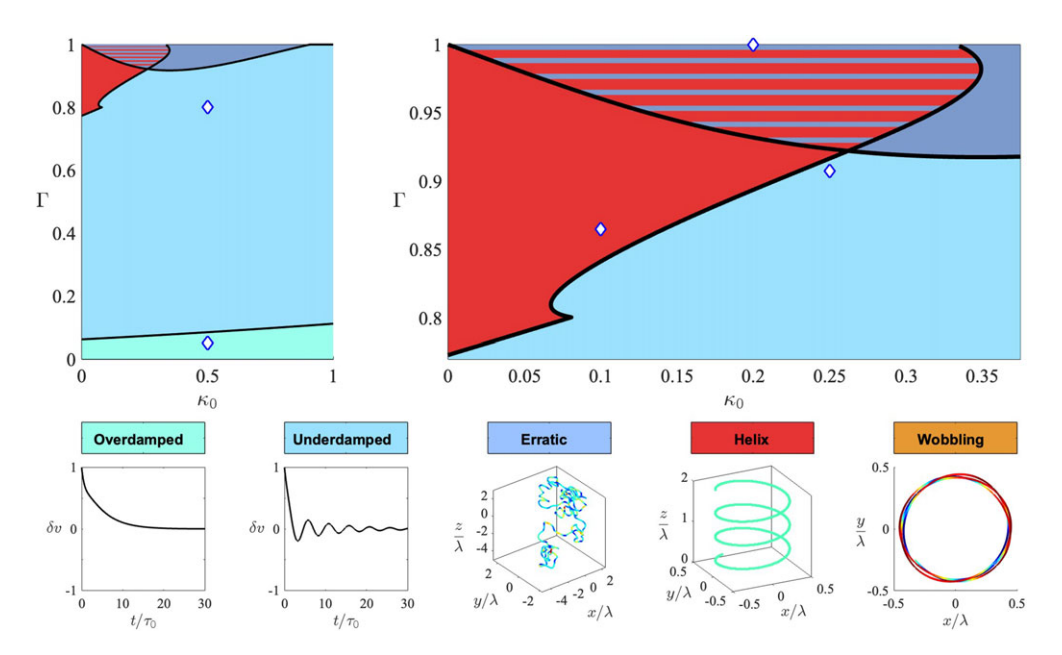


Figure 11. Regime diagram summarizing all the dynamical states identified in three dimensions. Plots of overdamped, underdamped and helical states have values of (κ_0, Γ) given by the diamonds in the corresponding coloured regions. The plots of erratic and wobbling states correspond to the diamonds at (0.2, 1) and (0.25, 0.90787), respectively.

Table 1. The dependence of classical pilot-wave dynamics on spatial dimension, β . With the three wave kernels specified, the dimensionless speed limits, c, are prescribed by $c = \sqrt{\beta}$, and the dependence of free particle speed u on the memory parameter $\Gamma = 1 - \mu$ is indicated. As time is non-dimensionalized by scaling with the memory time at the onset of propulsion, $\tau_0 = \sqrt{\beta DT/FAk^2}$, all three speed limits are equal to $\sqrt{FA/DT}$ in dimensional units.

	β	С	Wave kernel	Propulsion speed
1D	1	$\sqrt{1}$	cos(x)	$u = \sqrt{1 - \mu^2}$
2D	2	$\sqrt{2}$	$J_0(r)$	$u = \frac{1}{\sqrt{2}}\sqrt{4 - \mu^2 - \mu\sqrt{\mu^2 + 8}}$
3D	3	$\sqrt{3}$	j ₀ (r)	$u=(u^3/3)+\mu$ arctan u/μ

The self-propelling particle is accompanied by a quasi-monochromatic wave field. In pilot-wave hydrodynamics, the quasi-monochromatic form of the pilot wave is critical for the emergence of quantized orbits [7,36]. Specifically, it acts as a self-potential that serves to support only finite bands of orbital radii and so lead to orbital quantization [53]. We thus expect the basic paradigm for orbital quantization and the emergent quantum-like statistics in orbital pilot-wave dynamics in two dimensions to be robust to the extension to three dimensions. In hydrodynamic pilot-wave dynamics, underdamped in-line oscillations may give rise to the emergence of quantum-like statistics [11], so we expect this paradigm for quantum-like statistics to likewise arise in three-dimensional pilot-wave dynamics. On the basis of the similarities of the dynamics in two- and three-dimensional pilot-wave dynamics, we thus expect the two basic paradigms for the emergence of quantum-like behaviour in two dimensions [54] to persist in three dimensions.

There are also several notable differences with the two-dimensional dynamics. First, while solutions corresponding to planar spin states exist in both two and three dimensions, that with the smallest radius is stable in two dimensions, while all such states are unstable in three dimensions.

Second, the extra dimension allows for a novel phenomenon in the form of helical spin states that are quantized in both radius of curvature and pitch length. Specifically, like two-dimensional spin states [38], the helical spin states are quantized in radius of curvature by half wavelengths. A further quantization appears in the pitch length at half-integer multiples of the wavelength, resulting in a system with two 'quantum numbers' (n, ℓ) . We have assessed the stability of the helical spin states by examining their response to infinitesimal perturbations. All helical spin states above the lowest level (1,1) were found to be unstable in all parameter regimes considered. The stable helical spin state may coexist with rectilinear self-propelling states at relatively low particle inertia, or with erratic walkers for higher particle inertia. In the latter regime, the particle may follow an erratic trajectory for some time before spontaneously transitioning to a stable helical spin state. In this regime, since the rectilinear walking state is unstable, while the helical state is not, the default stable state thus changes from rectilinear walking to helical spin.

The spin of subatomic particles is widely believed to be a non-classical effect, an intrinsic feature with no known physical rationale. Attempts to provide such a rationale [55] are frequently based on physical pictures with some resemblance to the helical spin state. For example, classical models of the electron feature a charge executing a circular orbit with the Compton length at the Compton frequency, confined by its own electromagnetic field [56,57]. An inference that might be made from the field of hydrodynamic quantum analogues is that there is currently an unresolved quantum pilot-wave dynamics on the Compton time scale [3], analogous to the time scale of wave generation in our classical systems [2]. The helical spin state thus represents a beguiling new feature of classical pilot-wave dynamics that evokes classical models of the electron. If the dynamics is fully resolved, the particle is seen to follow a helical path in response to the constraint imposed by its pilot wave. However, if the scale of the pilot wave (and so of the helix diameter) were not resolved, one would instead infer motion, along the helix centreline, of an object with intrinsic angular momentum. The associated mean angular momentum vector is necessarily aligned either parallel or antiparallel to the direction of motion, but the instantaneous angular velocity necessarily precesses around its direction of motion. The dynamics of this multi-scale object will be the subject of future investigations.

Our extension to three dimensions will allow for an exploration of pilot-wave dynamics in a number of new settings inaccessible to either the hydrodynamic system or its parametric generalization. Of particular interest would be a characterization of orbital quantization in a central force, both a simple harmonic potential and a Coulomb potential, the latter of which promises a classical analogue of the hydrogen atom. The extensive studies of static and dynamic bound states in pilot-wave hydrodynamics, including crystals [58,59], and orbiting [60,61] and promenading pairs [62,63], might also be readily extended to include a third direction. The dynamic states arising from the interaction of helical spin states will also be characterized. Another potentially fruitful direction will be leveraging the analogy between a charge moving in a uniform magnetic field and a mass moving in a rotating frame [7]. The motion of a helical spin state in a rotating frame should thus bear some relation to that of a magnetic dipole in a uniform magnetic field.

As a final caveat, we note that our exploration of three-dimensional pilot-wave dynamics has been based on two assumptions. First, we have assumed a particular form of the wave kernel, $j_0(r)$, variation of which will undoubtedly change the stability characteristics of the various dynamical states. Second, our analysis is based on the stroboscopic approximation, which relies on the perfect resonance between the oscillations of the particle and its guiding wave form. Recent experimental work in pilot-wave hydrodynamics has revealed the importance of non-resonant effects, specifically the desynchronization of the bouncing drops and their pilot waves [47,64], which may alter the stability of various dynamical states. We expect that relaxing the assumption of resonance in our three-dimensional model through retention of the time oscillation of the wave kernel might likewise alter the stability of various dynamical states; for example, they might serve to stabilize both the helical and planar spin states. Consideration of different wave kernels and non-resonant effects will be the subject of future work.

Data accessibility. The code supporting this article has been uploaded as part of the electronic supplementary material [66].

Declaration of Al use. We have not used AI-assisted technologies in creating this article.

Authors' contributions. A.F.K.: formal analysis, funding acquisition, investigation, methodology, validation, visualization, writing—original draft and writing—review and editing; M.D.: formal analysis, investigation, methodology, supervision, writing—original draft and writing—review and editing; J.W.M.B.: conceptualization, funding acquisition, project administration, supervision, writing-original draft and writing—review and editing.

All authors gave final approval for publication and agreed to be held accountable for the work performed therein.

Conflict of interest declaration. We declare we have no competing interests.

Funding. A.F.K. gratefully acknowledges the Limitless Space Initiative for financial support through the LSI Postdoctoral Fellowship Program. J.W.M.B. also acknowledges the National Science Foundation for financial support through grant CMMI-2154151, and the Office of Naval Research through grant N000014-24-1-2232. Acknowledgements. The authors thank Nicholas Liu for insightful discussions.

Appendix A. Steady propulsion: linear stability analysis

To assess the linear stability of the walking state, we introduce a small impulse at t = 0, deviating the droplet from its steady motion. Following the framework developed by Oza et al. [29], we consider the perturbed trajectory equation

$$\kappa_0 \ddot{x}_p + \dot{x}_p = 3 \int_{-\infty}^t \frac{\mathbf{j}_1(|x_p(t) - x_p(s)|)}{|x_p(t) - x_p(s)|} (x_p(t) - x_p(s)) e^{-\mu(t-s)} \, \mathrm{d}s + \epsilon \delta(t), \tag{A1}$$

where $0 < \epsilon \ll 1$ is a small parameter governing the strength of the perturbation and $\delta(t) =$ $(c_{\parallel}e_{\parallel}+c_{\perp}e_{\perp})\delta(t)$ is a Dirac delta function with components parallel, e_{\parallel} , and perpendicular, e_{\perp} , to the steady motion, where c_{\parallel} and c_{\perp} are arbitrary O(1) constants. The influence of the small perturbation on the droplet path may be characterized by writing $x_p(t) = ute_{\parallel} + \epsilon x_1(t)H(t)$, where H(t) is the Heaviside function and $x_1(t) = x_{\parallel}(t)e_{\parallel} + x_{\perp}(t)e_{\perp}$ is the perturbed trajectory. Assuming continuity in the particle position across the Delta impulse, we deduce from (A 1) that $x_1(0) = 0$, with $\dot{x}_{\parallel}(0) = c_{\parallel}/\kappa_0$ and $\dot{x}_{\perp}(0) = c_{\perp}/\kappa_0$

To determine linearized evolution equations for the perturbed droplet motion parallel and perpendicular to the steady motion, we substitute the perturbation ansatz into (A1), expand nonlinear terms in powers of ϵ and retain only the leading-order terms. We deduce that

$$\kappa_0 \ddot{x}_{\parallel} + \dot{x}_{\parallel} = 3 \left[x_{\parallel} \int_0^{\infty} g_{\parallel}(s) \, \mathrm{d}s - (x_{\parallel} * g_{\parallel}) \right]$$
(A 2a)

and

$$\kappa_0 \ddot{x}_\perp + \dot{x}_\perp = 3 \left[x_\perp \int_0^\infty g_\perp(s) \, \mathrm{d}s - (x_\perp * g_\perp) \right],\tag{A 2b}$$

where

$$g_{\parallel}(t) = j'_{1}(ut)e^{-\mu t}$$
 and $g_{\perp}(t) = \frac{j_{1}(ut)}{ut}e^{-\mu t}$

account for the influence of path memory on the particle motion, with * denoting the convolution $(f * g)(t) = \int_0^t f(s)g(t-s) ds$. Notably, one may integrate by parts and apply the relationship (2.5) to evaluate the coefficient of x_{\parallel} in (A 2a), giving $\int_{0}^{\infty} g_{\parallel}(s) ds = \frac{1}{3}\mu$. We thus observe that this component of the wave force, which acts as a repelling spring, serves to perturb the particle from its steady motion; however, our analysis below indicates that this effect is countered by the convolution term, which may dampen inline perturbations when the path memory remains below a critical threshold.

To investigate the long-time response of particle motion to perturbation, we analyse the equations for $\widehat{X}_{\parallel}(s) = \mathcal{L}[x_{\parallel}](s)$ and $\widehat{X}_{\perp}(s) = \mathcal{L}[x_{\perp}](s)$, where $\mathcal{L}[f](s) = \int_{0}^{\infty} f(t)e^{-st} dt$ denotes the Laplace transform. Specifically, we deduce that $\widehat{X}_{\parallel}(s) = c_{\parallel}/F_{\parallel}(s)$ and $\widehat{X}_{\perp}(s) = c_{\perp}/F_{\perp}(s)$, where the

transfer functions are defined

$$F_{\parallel}(s) = \kappa_0 s^2 + s - \mu + 3\widehat{g}_{\parallel}(s)$$
 and $F_{\perp}(s) = \kappa_0 s^2 + s - 3\widehat{g}_{\perp}(0) + 3\widehat{g}_{\perp}(s)$, (A3)

with

$$\widehat{g}_{\parallel}(s) = \frac{(\mu + s)}{u^2} \left[1 - \frac{(\mu + s)}{u} \arctan\left(\frac{u}{\mu + s}\right) \right] \quad \text{and} \quad \widehat{g}_{\perp}(s) = \mathcal{L}[g_{\perp}](s)$$

being the Laplace transforms of g_{\parallel} and g_{\perp} , respectively. The roots of each transfer function determine the long-time response of the particle to perturbations from steady motion: specifically, the motion is stable when all roots lie in the left-half plane, with the magnitude of all perturbations decaying exponentially in time, and unstable otherwise. Owing to the relative complexity of the algebraic expressions describing the transfer functions, we compute all roots numerically using the method of Delves & Lyness [65]. Although $\widehat{g}_{\perp}(s)$ may be evaluated analytically, we omit its form for the sake of brevity.

Appendix B. Helical states: linear stability analysis

The constants, a_{ij} , and functions, $b_{ij}(t)$, appearing in (3.6) are defined

$$\begin{split} a_{11} &= \mathscr{I}[f_1(t) - r_0^2 f_2(t)(1 - \cos \omega t)^2], \\ a_{12} &= \mathscr{I}[f_1(t) \sin(\omega t) - r_0^2 f_2(t)(1 - \cos \omega t) \sin(\omega t)], \\ a_{13} &= -r_0 v \mathscr{I}[f_2(t)t(1 - \cos \omega t)], \\ a_{21} &= -r_0^2 \mathscr{I}[f_2(t)(1 - \cos \omega t) \sin(\omega t)], \\ a_{22} &= \mathscr{I}[f_1(t) \cos(\omega t) - r_0^2 f_2(t) \sin^2(\omega t)], \\ a_{23} &= -r_0 v \mathscr{I}[f_2(t)t \sin(\omega t)], \\ a_{31} &= -r_0 v \mathscr{I}[f_2(t)t \sin(\omega t)], \\ a_{32} &= -r_0 v \mathscr{I}[f_2(t)t \sin(\omega t)], \\ a_{33} &= \mathscr{I}[f_1(t) - v^2 t^2 f_2(t)], \end{split}$$

and

and

$$b_{11}(t) = -f_1(t)\cos(\omega t) - r_0^2 f_2(t)(1 - \cos \omega t)^2,$$

$$b_{12}(t) = -f_1(t)\sin(\omega t) + r_0^2 f_2(t)(1 - \cos \omega t)\sin(\omega t),$$

$$b_{13}(t) = r_0 v f_2(t) t (1 - \cos \omega t),$$

$$b_{21}(t) = f_1(t)\sin(\omega t) - r_0^2 f_2(t)(1 - \cos \omega t)\sin(\omega t),$$

$$b_{22}(t) = -f_1(t)\cos(\omega t) + r_0^2 f_2(t)\sin^2(\omega t),$$

$$b_{23}(t) = r_0 v f_2(t) t \sin(\omega t),$$

$$b_{31}(t) = -r_0 v f_2(t) t \sin(\omega t),$$

$$b_{32}(t) = r_0 v f_2(t) t \sin(\omega t)$$

$$b_{33}(t) = -f_1(t) + v^2 t^2 f_2(t),$$

and

where $\mathscr{I}[f(t)] = \int_0^\infty f(t) dt$,

$$f_1(t) = \frac{j_1(\mathcal{D}(t))}{\mathcal{D}(t)} e^{-\mu t}, \quad f_2(t) = \frac{j_2(\mathcal{D}(t))}{\mathcal{D}^2(t)} e^{-\mu t} \quad \text{and} \quad \mathcal{D}(t) = \sqrt{2r_0^2(1 - \cos(\omega t)) + v^2 t^2}$$

is the distance between the particle and its position a time *t* in the past.

References

- 1. Couder Y, Protière S, Fort E, Boudaoud A. 2005 Walking and orbiting droplets. *Nature* 437, 208. (doi:10.1038/437208a)
- Bush JWM. 2015 Pilot-wave hydrodynamics. Ann. Rev. Fluid Mech. 47, 269–292. (doi:10.1146/annurev-fluid-010814-014506)
- 3. Bush JWM, Oza AU. 2021 Hydrodynamic quantum analogs. *Rep. Prog. Phys.* **84**, 017001. (doi:10.1088/1361-6633/abc22c)
- 4. Couder Y, Fort E. 2006 Single particle diffraction and interference at a macroscopic scale. *Phys. Rev. Lett.* **97**, 154101. (doi:10.1103/PhysRevLett.97.154101)
- 5. Pucci G, Harris DM, Faria LM, Bush JWM. 2018 Walking droplets interacting with single and double slits. *J. Fluid Mech.* **835**, 1136–1156. (doi:10.1017/jfm.2017.790)
- 6. Ellegaard C, Levinsen MT. 2020 Interaction of wave-driven particles with slit structures. *Phys. Rev. E* **102**, 023115. (doi:10.1103/PhysRevE.102.023115)
- 7. Fort E, Eddi A, Moukhtar J, Boudaoud A, Couder Y. 2010 Path-memory induced quantization of classical orbits. *Proc. Natl Acad. Sci. USA* **107**, 17515–17520. (doi:10.1073/pnas.1007386107)
- 8. Harris DM, Bush JWM. 2014 Drops walking in a rotating frame: from quantized orbits to multimodal statistics. *J. Fluid Mech.* **739**, 444–464. (doi:10.1017/jfm.2013.627)
- 9. Oza AU, Wind-Willassen O, Harris DM, Rosales RR, Bush JWM. 2014 Pilot-wave hydrodynamics in a rotating frame: exotic orbits. *Phys. Fluids* **26**, 082101. (doi:10.1063/1.4891568)
- 10. Perrard S, Labousse M, Miskin M, Fort E, Couder Y. 2014 Self-organization into quantized eigenstates of a classical wave-driven particle. *Nat. Comm.* **5**, 3219. (doi:10.1038/ncomms4219)
- 11. Sáenz PJ, Cristea-Platon T, Bush JWM. 2018 Statistical projection effects in a hydrodynamic pilot-wave system. *Nat. Phys.* **14**, 315–319. (doi:10.1038/s41567-017-0003-x)
- 12. Sáenz PJ, Cristea-Platon T, Bush JWM. 2020 A hydrodynamic analog of Friedel oscillations. *Sci. Adv.* **6**, 9234. (doi:10.1126/sciadv.aay9234)
- 13. Papatryfonos K, Ruelle M, Bourdiol C, Nachbin A, Bush JWM, Labousse M. 2022 Hydrodynamic superradiance in wave-mediated cooperative tunneling. *Commun. Phys.* 5, eaay142. (doi:10.1038/s42005-022-00918-y)
- 14. Abraham AJ, Malkov S, Ljubetic FA, Durey M, Sáenz PJ. 2024 Anderson localization of walking droplets. *Phys. Rev. X* 14, 031047. (doi:10.1103/PhysRevX.14.031047)
- 15. Frumkin V, Darrow D, Bush JWM, Struyve W. 2022 Real surreal trajectores in pilot-wave hydrodynamics. *Phys. Rev. A* **106**, L010203. (doi:10.1103/PhysRevA.106.L010203)
- Frumkin V, Bush JWM. 2023 Misinference of interaction-free measurement from a classical system. *Phys. Rev. A* 108, L060201. (doi:10.1103/PhysRevA.108.L060201)
- 17. de Broglie L. 1987 Interpretation of quantum mechanics by the double solution theory. *Ann. Fond. Louis Broglie* **12**, 1–23.
- 18. de la Peña L, Cetto AM, Valdés-Hernández A. 2015 The emerging quantum: the physics behind quantum mechanics. Cham, Switzerland: Springer.
- 19. Dagan Y, Bush JWM. 2020 Hydrodynamic quantum field theory: the free particle. *C. R. Mécanique* **348**, 552–570. (doi:10.5802/crmeca.34)
- 20. Durey M, Bush JWM. 2020 Hydrodynamic quantum field theory: the onset of particle motion and the form of the pilot wave. *Front. Phys.* **8**, 300. (doi:10.3389/fphy.2020.00300)
- 21. Drezet A, Jamet P, Bertschy D, Ralko A, Poulain C. 2020 Mechanical analog of quantum bradyons and tachyons. *Phys. Rev. E* **102**, 052206. (doi:10.1103/PhysRevE.102.052206)
- 22. Darrow D, Bush JWM. 2024 Revisiting de Broglie's double-solution pilot-wave theory with a Lorentz-covariant Lagrangian framework. *Symmetry* **16**, 149. (doi:10.3390/sym16020149)
- 23. Le Gal P, Castillo Morales B, Hernandez Zapata S, Ruiz Chavarria G. 2022 Swimming of a ludion in a stratified sea. *J. Fluid Mech.* **931**, A14. (doi:10.1017/jfm.2021.931)
- Mei CC, Zhou X. 1991 Parametric resonance of a spherical bubble. J. Fluid Mech. 229, 29–50. (doi:10.1017/S0022112091002926)
- 25. Roux A, Martischang JP, Baudoin M. 2022 Self-radiation force on a moving monopolar source. *J. Fluid Mech.* **952**, A22. (doi:10.1017/jfm.2022.920)
- Turton SE, Couchman MMP, Bush JWM. 2018 A review of the theoretical modeling of walking droplets: towards a generalized pilot-wave framework. *Chaos* 28, 096111. (doi:10.1063/1.5032221)
- 27. Moláček J, Bush JWM. 2013 Droplets bouncing on a vibrating fluid bath. J. Fluid Mech. 727, 582–611. (doi:10.1017/jfm.2013.279)

- 28. Moláček J, Bush JWM. 2013 Drops walking on a vibrating bath: towards a hydrodynamic pilot-wave theory. J. Fluid Mech. 727, 612–647. (doi:10.1017/jfm.2013.280)
- 29. Oza AU, Rosales RR, Bush JWM. 2013 A trajectory equation for walking droplets: hydrodynamic pilot-wave theory. *J. Fluid Mech.* 737, 552–570. (doi:10.1017/jfm.2013.581)
- 30. Harris DM, Quintela J, Prost V, Brun PT, Bush JWM. 2017 Visualization of hydrodynamic pilot-wave phenomena. *J. Vis.* **20**, 13–15. (doi:10.1007/s12650-016-0383-5)
- 31. Durey M, Turton SE, Bush JWM. 2020 Speed oscillations in classical pilot-wave dynamics. *Proc. Roy. Soc. A* **476**, 20190884. (doi:10.1098/rspa.2019.0884)
- 32. Durey M. 2020 Bifurcations and chaos in a Lorenz-like pilot-wave system. *Chaos* 30, 103115. (doi:10.1063/5.0020775)
- 33. Wind-Willassen O, Moláček J, Harris DM, Bush JWM. 2013 Exotic states of bouncing and walking droplets. *Phys. Fluids* **25**, 1–11. (doi:10.1063/1.4817612)
- 34. Bacot V, Perrard S, Labousse M, Couder Y, Fort E. 2019 Multistable free states of an active particle from a coherent memory dynamics. *Phys. Rev. Lett.* **122**, 104303. (doi:10.1103/Phys RevLett.122.104303)
- 35. Hubert M, Labousse M, Perrard S, Labousse M, Vandewalle N, Couder Y. 2019 Tunable bimodal explorations of space from memory-driven deterministic dynamics. *Phys. Rev. E* **100**, 032201. (doi:10.1103/PhysRevE.100.032201)
- 36. Oza AU, Harris DM, Rosales RR, Bush JWM. 2014 Pilot-wave dynamics in a rotating frame: on the emergence of orbital quantization. *J. Fluid Mech.* **744**, 404–429. (doi:10.1017/jfm.2014.50)
- 37. Bernard-Bernardet S, Fleury M, Fort E. 2022 Spontaneous emergence of a spin state for an emitter in a time-varying medium. *Eur. Phys. J. Plus* **137**, 432. (doi:10.1140/epjp/s13360-022-02646-2)
- 38. Oza AU, Rosales RR, Bush JWM. 2018 Hydrodynamic spin states. *Chaos* **28**, 096106. (doi:10.1063/1.5034134)
- Durey M, Bush JWM. 2021 Classical pilot-wave dynamics: the free particle. *Chaos* 31, 033136. (doi:10.1063/5.0039975)
- 40. Valani R, Slim AC. 2018 Pilot-wave dynamics of two identical, in-phase bouncing droplets. *Chaos* 28, 096114. (doi:10.1063/1.5032128)
- 41. Valani R, Slim AC, Simula T. 2018 Hong-Ou-Mandel-like two-drop correlations. *Chaos* 28, 096104. (doi:10.1063/1.5032114)
- 42. Tambasco LD, Bush JWM. 2018 Exploring orbital dynamics and trapping with a generalized pilot-wave framework. *Chaos* **28**, 096115. (doi:10.1063/1.5033962)
- 43. Eddi A, Sultan E, Moukhtar J, Fort E, Rossi M, Couder Y. 2011 Information stored in Faraday waves: the origin of a path memory. *J. Fluid Mech.* 674, 433–463. (doi:10.1017/S002 2112011000176)
- 44. Milewski P, Galeano-Rios C, Nachbin A, Bush JWM. 2015 Faraday pilot-wave dynamics: modelling and computation. *J. Fluid Mech.* 778, 361–388. (doi:10.1017/jfm.2015.386)
- 45. Durey M, Milewski PA. 2017 Faraday wave-droplet dynamics: discrete-time analysis. *J. Fluid Mech.* **821**, 296–329. (doi:10.1017/jfm.2017.235)
- Tadrist L, Shim JB, Gilet T, Schlagheck P. 2018 Faraday instability and subthreshold Faraday waves: surface waves emitted by walkers. J. Fluid Mech. 848, 906–945. (doi:10.1017/jfm.2018.358)
- 47. Couchman MMP, Turton SE, Bush JWM. 2019 Bouncing phase variations in pilot-wave hydrodynamics and the stability of droplet pairs. *J. Fluid Mech.* **871**, 212–243. (doi:10.1017/jfm.2019.293)
- 48. Galeano-Rios CA, Couchman MMP, Caldairou P, Bush JWM. 2018 Ratcheting droplet pairs. *Chaos* 28, 096112. (doi:10.1063/1.5032116)
- 49. Papatryfonos K, Vervoort L, Nachbin A, Labousse M, Bush JWM. 2024 Static Bell test in pilotwave hydrodynamics. *Phys. Rev. Fluids* **9**, 084001. (doi:10.1103/PhysRevFluids.9.084001)
- 50. Valani R, Slim AC, Paganin DM, Simula TP, Vo T. 2021 Unsteady dynamics of a classical particle-wave entity. *Phys. Rev. E* **104**, 015106. (doi:10.1103/PhysRevE.104.015106)
- 51. Labousse M, Perrard S, Couder Y, Fort E. 2016 Self-attraction into spinning eigenstates of a mobile wave source by its emission back-reaction. *Phys. Rev. E* **94**, 042224. (doi:10.1103/Phys RevE.94.042224)
- 52. Perrard S, Labousse M, Fort E, Couder Y. 2014 Chaos Driven by Interfering Memory. *Phys. Rev. Lett.* **113**, 104101. (doi:10.1103/PhysRevLett.113.104101)
- 53. Liu N, Durey M, Bush JWM. 2023 Pilot-wave dynamics in a rotating frame: the onset of orbital instability. *J. Fluid Mech.* 973, A4. (doi:10.1017/jfm.2023.742)

- Bush JWM, Frumkin V, Sáenz PJ. 2024 Perspectives on pilot-wave hydrodynamics. *Appl. Phys. Lett.* 125, 030503. (doi:10.1063/5.0210055)
- 55. Ohanian HC. 1986 What is spin? Am. J. Phys. 54, 500–505. (doi:10.1119/1.14580)
- 56. Burinskii A. 2008 The Dirac-Kerr-Newman electron. *Gravit. Cosmol.* **14**, 109–122. (doi:10.1134/S0202289308020011)
- 57. Hestenes D. 1990 The zitterbewegung interpretation of quantum mechanics. *Found. Phys.* **20**, 1213–1232. (doi:10.1007/BF01889466)
- 58. Eddi A, Decelle A, Fort E, Couder Y. 2009 Archimedean lattices in the bound states of wave interacting particles. *Europhys. Lett.* **87**, 56002. (doi:10.1209/0295-5075/87/56002)
- 59. Couchman MMP, Bush JWM. 2020 Free rings of bouncing droplets: stability and dynamics. *J. Fluid Mech.* **903**, A49. (doi:10.1017/jfm.2020.648)
- 60. Protière S, Boudaoud A, Couder Y. 2006 Particle-wave association on a fluid interface. *J. Fluid. Mech.* 554, 85–108. (doi:10.1017/S0022112006009190)
- 61. Oza AU, Siéfert E, Harris DM, Moláček J, Bush JWM. 2017 Orbiting pairs of walking droplets: dynamics and stability. *Phys. Rev. Fluids* **2**, 053601. (doi:10.1103/PhysRevFluids.2.053601)
- 62. Borghesi C, Moukhtar J, Labousse M, Eddi A, Fort E, Couder Y. 2014 Interaction of two walkers: wave-mediated energy and force. *Phys. Rev. E* **90**, 063017. (doi:10.1103/Phys RevE.90.063017)
- 63. Arbelaiz J, Oza AU, Bush JWM. 2018 Promenading pairs of walking droplets: dynamics and stability. *Phys. Rev. Fluids* **3**, 013604. (doi:10.1103/PhysRevFluids.3.013604)
- 64. Primkulov BK, Evans DJ, Been JB, Bush JWM. 2025 Non-resonant effects in pilot-wave hydrodynamics. *Phys. Rev. Fluids* **10**, 013601. (doi:10.1103/PhysRevFluids.10.013601)
- 65. Delves LM, Lyness JN. 1967 A numerical method for locating the zeros of an analytic function. *Math. Comput.* **21**, 543–560. (doi:10.1090/S0025-5718-1967-0228165-4)
- 66. Kay AF, Durey M, Bush JWM. 2025 Classical pilot-wave dynamics in three dimensions. Figshare. (doi:10.6084/m9.figshare.c.7929110)